Journal of Electroanalytical Chemistry 765 (2016) 45–51

Contents lists available at ScienceDirect

Journal of Electroanalytical Chemistry

journal homepage: www.elsevier.com/locate/jelechem

EQCM study of oxygen cathodes in DMSO $LiPF_6$ electrolyte

W.R. Torres, L. Cantoni, A.Y. Tesio, M. del Pozo, E.J. Calvo *

INQUIMAE, Facultad de Ciencias Exactas y Naturales, Pabellón 2, Ciudad Universitaria, AR-1428 Buenos Aires, Argentina

ARTICLE INFO

Article history:
Received 2 June 2015
Received in revised form 27 July 2015
Accepted 28 July 2015
Available online 17 August 2015

Keywords:
Lithium
Oxygen
Battery
EQCM
DMSO

ABSTRACT

The oxygen reduction reaction (ORR) in DMSO containing $LiPF_6$ has been studied with the electrochemical quartz crystal microbalance (EQCM) during galvanostatic cathodic and anodic pulses, chronoamperometry and cyclic voltammetry experiments. We disclose here for the first time gravimetric evidence with the EQCM of the different mechanistic models that apply to the ORR in $LiPF_6$/DMSO electrolyte: (i) Surface electrochemical/chemical deposition of Li_2O_2(s) and (ii) solution phase disproportion of LiO_2(soln) yields large Li_2O_2 particles. The mass per electron detected with the EQCM depends on the respective current rates and thus on the mechanisms, i.e. 23 g/F for the formation of Li_2O_2 thin film at high current density and much larger values for low current density due to solvent co-deposition and further degradation.

1. Introduction

The rechargeable lithium-air battery exhibits a very large theoretical energy density that can compete with fossil fuels for electric vehicle applications with extended millage range [1–5]. In the non-aqueous Li-air battery introduced by Abraham and Jiang [6], during discharge a lithium metal anode dissolves in non-aqueous electrolyte and the resulting Li^+ ions react with oxygen reduction products to form insoluble lithium peroxide Li_2O_2 at a porous carbon cathode as shown unambiguously by Laoire et.al. using XRD [7]. The first report of the unique O_2 reduction reaction (ORR) chemistry in lithium ion containing DMSO was reported by Laoire et.al. [8]. Bruce et.al. [9] confirmed that the electrochemical reaction of Li^+ with oxygen to yield insoluble Li_2O_2 in non-aqueous electrolyte is reversible. Bruce [10] further claimed that the Li-air battery in DMSO [8,11,12], with a very large dipolar moment ($\mu = 4{,}3$ D), can be recharged with 95% capacity retention in 100 cycles using DMSO electrolyte and porous gold electrode. There is a controversy on the stability of DMSO in the presence of oxygen reduction reaction (ORR) products [13] in particular when the electrode area to electrolyte volume is high [14]. Furthermore, solid $LiPF_6$ has been observed to react with solid Li_2O_2 by XPS [15].

Two different models have been proposed for the ORR in lithium containing non-aqueous solvents [16–19]: (a) a surface reaction mechanism leading to thin Li_2O_2 films, and (b) a solution phase mechanism via disproportion of soluble lithium superoxide with formation of large Li_2O_2 particles.

The surface mechanism is favored at high current densities and low donor number solvent thin film growth with passivation of the active cathode:

$$O_2 + Li^+ + e \rightarrow [O_2Li]_{surf} \quad (1)$$

$$[O_2Li]_{surf} + [O_2Li]_{surf} \rightarrow Li_2O_{2\downarrow} + O_2 \quad (2)$$

$$[O_2Li]_{surf} + Li^+ + e \rightarrow Li_2O_{2\downarrow}. \quad (3)$$

While the solution phase mechanisms prevails at low current density and high donor number solvents:

$$O_2 + Li^+ + e \rightarrow [O_2Li]_{soln} \quad (4)$$

$$2[O_2Li]_{soln} \rightarrow Li_2O_{2\downarrow}(\text{particle}) + O_2. \quad (5)$$

The morphology of the main discharge product of ORR in lithium containing non-aqueous electrolyte strongly depends on the solvent and current density which define the possible surface and solution phase mechanisms [20]. In the first case Li_2O_2 thin film passivates the electrode active surface while the solution mechanism involves diffusion of soluble LiO_2 and disproportion with precipitation of Li_2O_2 into discs or toroid particles [21].

Both mechanisms predict that the mass of Li_2O_2 per mol of electrons (mpe) expected from reaction (2) or reaction (4) is 23 g per mol-e, while mpe for reaction (1) is 39 and for reaction (3) is 7 g per mol-e [14,22]. Jie and Uosaki [22] have recently reported electrochemical quartz crystal microbalance (EQCM), studies of O_2 reduction in $LiPF_6$-DMSO electrolyte deposition on a gold electrode. These authors reported the mpe calculated from the slope of a mass-to-charge plot of

* Corresponding author.
E-mail address: calvo@qi.fcen.uba.ar (E.J. Calvo).

http://dx.doi.org/10.1016/j.jelechem.2015.07.046
1572-6657/

37 g/mol-e in a very limited potential window, suggesting deposition of lithium superoxide. Aurbach et.al. [14,23] reported on similar EQCM studies with an mpe of 22 g/mol-e in the limited voltage interval of 2.7 to 2.3 V and larger values that correspond to DMSO decomposition products of larger molar mass.

Rotating ring disc electrode (RRDE) study has not detected soluble superoxide ion in 0.1 M $LiPF_6$/acetonitrile [12]. However, at very low $LiClO_4$ concentrations, c.a. 10 μM, traces of soluble O_2^- have been detected downstream at the ring electrode of a RRDE system [24]. Soluble LiO_2 has also been detected at the ring electrode in acetonitrile 0.1 M lithium electrolyte with small amounts of DMSO added [12]; with the O_2^- oxidation ring current exhibiting a maximum due competing reactions (4) and (5) [12,24,25]. Furthermore, re-oxidation of O_2^- can be detected in fast cyclic voltammetry with limited cathodic excursion so that further reduction or disproportion of superoxide is avoided [26]. The preferential solvation of Li^+ by DMSO molecules is also reflected in the lower electrode potential of Li/Li^+ in DMSO with respect to low donor number acetonitrile by 0.5 V [27]. In a recent communication of rotating ring disc electrode (RRDE) and electrochemical quartz crystal microbalance (EQCM) study of ORR in $LiPF_6$/DMSO under a burst of soluble lithium superoxide oxidation measured by the ring current at short times has been described in coincidence with a time lag in the mass uptake by the EQCM [28]. This has been interpreted as a result of soluble superoxide concentration build up at the cathode surface followed by disproportion in solution.

In the present study we have carried out careful EQCM experiments during the ORR on Au electrodes in $LiPF_6$ and DMSO electrolytes in order to determine the weight gained due to the formation of an insoluble deposit [14] which passivates the electrode surface [12].

2. Experimental

2.1. Chemicals

Anhydrous dimethyl sulfoxide (DMSO), ≥99.9%, anhydrous acetonitrile ≥99.8%, $LiPF_6$ battery grade, ≥99.99% were obtained from SIGMA-ALDRICH and stored in the argon-filled MBRAUN glove box with the oxygen content of ≤0.1 ppm and water content below 2 ppm. Acetonitrile and DMSO were dried for several days over molecular sieves, 3 Å (SIGMA-ALDRICH). All solutions were prepared inside the glove box and the water content was measured using the Karl Fisher 831 KF Coulometer (Metrohm) with typically 30 ppm of water at the beginning of the experiment. After few hours of experimentation even with precautions the lithium salt in DMSO absorbs water from the ambient and Karl Fischer measurements resulted in a content of water as high as 2000–3000. Since long term experiments in lithium electrolyte accumulated water from the ambient, short term experiments with freshly prepared solutions and short exposure to dry air were preferred.

The electrochemical cell was built all in Teflon® and the 10 MHz quartz crystal (Intl. Crystal Manufacturer, Oklahoma) were coated with 0.2 cm^2 gold discs (with 200 nm Au on titanium adhesion layer), placed at the bottom and filled with the electrolyte. Dupont™ Kalrez perfluoro elastomeric AS568 o-rings were used in acetonitrile and DMSO solutions. A non-aqueous reference electrode made with a Pt wire coated with equimolar $LiMn_2O_4/LiMn_2O_4$ [29] in the same electrolyte was used in a fritted glass compartment. The electrode potential of 3.25 V vs. Li/Li^+ (3.2 mm diameter Li wire, 99.9% trace metals basis SIGMA-ALDRICH, in the Ar filled glove box, in contact with 0.1 $LiPF_6$ in DMSO) was measured, and all potentials herein are referred to the Li/Li^+ scale. A 1 cm^2 platinum gauze (Johnson Matthey) was employed as counter electrode.

Crystal admittance spectra in the vicinity of the fundamental resonant frequency, f_o, were acquired using a Hewlett Packard HP E5100A network analyzer connected to the quartz crystal in the Teflon electrochemical cell through 50 Ω coaxial matched cables (HP10502A) via a HP 41900A Π-Network test fixture with rigid brass connectors to the crystal. The HP E5100A network analyzer was interfaced to a computer via Agilent 82357B USB/GPIB interface and the electrochemical cell was controlled with a grounded working electrode by means of an operational amplifier potentiostat/galvanostat with special software developed in the laboratory using Labview 10.0 (National Instruments). The high frequency circuit connecting the grounded working electrode was isolated by means of a series 4.7 nF capacitor, the electrochemical current was measured at the auxiliary electrode and both current and potential signals were acquired by 2 Agilent 34410 $6^{1/2}$ digit multimeters by USB interfaces. The network analyzer was calibrated prior to each measurement by 3-term calibration: open, close and 50 Ω. The acoustic admittance spectra of the Au covered quartz crystal were recorded at 1.5 s intervals simultaneous to current and potential signals for oxygen reduction reaction (ORR).

2.2. Theory of EQCM

In order to analyze the thickness shear mode resonator (TSM) loaded with a Li_2O_2 deposit and immersed in the liquid DMSO electrolyte, we used the lumped element model (LEM) of the modified Buterworth van Dyke (BVD) circuit [30] for which the surface mechanical impedance Z_{LEM} is given by the following [30,31]:

$$Z(LEM) = \frac{\phi_q(Z_S/Z_q)}{4K^2\omega C_o}\left[1 - \frac{j(Z_S/Z_q)}{2\tan\left(\phi_q/2\right)}\right]^{-1} \tag{6}$$

where K^2 is the quartz electromechanical coupling coefficient, ϕ is the complex acoustic wave phase shift across the quartz, C_o is the static capacitance of the resonator, $\omega = 2\pi f$ with f the excitation frequency, where Z_q is the quartz characteristic impedance $Z_q = \sqrt{(\rho_q \mu_q)}$, ρ_q is the quartz density (2651 kg m^{-3}) and μ_q the quartz stiffness ($2.947 \cdot 10^{10}$ N·m^{-2}), Z_S is the surface mechanical impedance due to the surface ORR insoluble products and viscous DMSO liquid in contact with it while Z_q for AT cut quartz crystal is $8.849 \cdot 10^6$ kg m^{-2} s^{-1}. Near resonance $\omega \cong \omega_o$ where $\omega_o = 2\pi f_o$, with f_o the series resonance frequency and N the harmonic resonance [32]. If $|Z_S|/Z_q \ll 2 \cdot \tan(\phi_q/2)$ the Z_{LEM} can be approximated by the following [33]:

$$Z_{LEM} \cong \frac{N\pi}{4K^2\omega_S C_O}\left(\frac{Z_S}{Z_q}\right) = R_S + jX_{LS} \tag{7}$$

where R_S and X_{LS} are the real and imaginary parts of the lumped element impedance Z_{LEM}.

The validity of the LEM equivalent circuit to within 1% of the Transmission Line Model [30] is fulfilled for the ratio of the surface film and/or liquid impedance (Z_S) to the quartz crystal impedance (Z_Q) $Z_S/Z_Q < 0.005$, i.e. since $Z_q \sim 535{,}000$ Ω this holds for $Z_S \leq 2675$ Ω. This condition is fulfilled in the present work.

If a non-piezoelectric layer is attached to the crystal and covered by a viscous liquid much thicker than the acoustic wave penetration (semi-infinite liquid), the surface impedance Z_S is given by the following [34]:

$$Z_S = \left[\frac{Z_f^* \tanh(k_f d_f) + Z_l^*}{1 + \frac{Z_l^*}{Z_f^*}\tanh(k_f d_f)}\right] \tag{8}$$

where the subscript "f" denotes the viscoelastic film under-layer and "l" the liquid over layer respectively. The characteristic film and liquid impedances are respectively Z_f^* and Z_l^*; and k_f the film complex wave propagation constant $k_f = j\omega(\rho_f / G_f)^{1/2}$. And, thus the Z_S of a viscoelastic film on a quartz crystal immersed in liquid depends on the liquid density (ρ_l) and viscosity (η_l) and the film thickness (d_f), density (ρ_f) and shear (storage G'_f and loss G''_f moduli with the complex shear modulus is $G = G' + jG''$ and the characteristic film impedance is $Z_f^* = \sqrt{(G_f \rho_f)}$).

Therefore Eqs. (7) and (8) show that both R_f and X_L grow with the viscoelastic film mass and thickness increase. On the other hand, the characteristic mechanical impedance of the Newtonian liquid is as follows:

$$Z_1^* = \sqrt{\rho_1\eta_l\omega j} = (1+j)\sqrt{\frac{\rho_1\eta_l\omega}{2}} \tag{9}$$

and thus $R_l = X_{Ll}$ for a Newtonian viscous liquid on the bare quartz crystal. For DMSO $\rho = 1.104\ g{\cdot}cm^{-3}$ $\eta = 1.196\ cm^2{\cdot}s^{-1}$ so the electrical impedance of the quartz crystal immersed in the viscous DMSO liquid is $Z_L^* = 326\ \Omega$. For the 0.1 M $LiPF_6$/DMSO electrolyte solution with the 10 MHz quartz crystal mounted with the o-ring we find experimentally 460 Ω.

The electrical complex admittance of the BVD equivalent electrical circuit of Fig. 1 is as follows:

$$Y(\omega) = G(\omega) + jB(\omega) \tag{10}$$

where the real part $G(\omega)$ is the conductance and the imaginary part $B(\omega)$ the susceptance of the quartz crystal admittance is given in terms of the BVD [35]:

$$G = \frac{R}{R^2 + \left(\omega L - \frac{1}{\omega C}\right)^2} \text{ and } B = \omega C_o - \frac{\left(\omega L - \frac{1}{\omega C}\right)}{R^2 + \left(\omega L - \frac{1}{\omega C}\right)^2}. \tag{11}$$

With $j = \sqrt{-1}$ and $\omega_o = 2\pi f_o$ defines de series resonant frequency of the quartz crystal with a maximum conductance $G(\omega_o)_{max} = 1/R$ at the resonant frequency. The conductance G and susceptance B of the piezoelectric quartz crystal resonator were measured with HP5100A network analyzer in transmission mode as a function of frequency around the series resonance frequency ($\omega_S = 2\pi f_s$) at which the motional resistance is cero. Simultaneous fits of the admittance spectra to $G(\omega)$ and $B(\omega)$ for the modified LEM BVD equivalent circuit equations using Levemberg–Marquardt routine written in Labview 10.0 environment were performed to obtain values of ωL and R.

The resistance, R, represents all the losses of energy of the shear wave penetrating the liquid and surface film as well as losses in the o-ring support. Typical values of Rq = 40 Ω (including o-ring and crystal fitting), Lq = 8.5 mH, Cq = 30 fF, and C_0 = 1 pF for 10 MHz crystals in air with ωL (total) ~ 535,000 Ω were obtained and experimentally verified.

For low crystal load by the surface deposit ($Z_L \ll Z_Q$) a lumped element circuit can be approximated and the shift in the quartz impedance due to the ORR products deposit can be written as follows:

$$\Delta Z = \Delta R + j\Delta(\omega L) \tag{12}$$

where ΔR and Δ(ωL) are the real and imaginary parts of the impedance shift with respect to the initial quartz crystal condition before the beginning of the ORR process. The Saurbrey equation relates the resonant frequency shift with the areal mass of deposit [36]:

$$\Delta f = -\frac{\left(2f_0^2\right)}{\sqrt{(\rho_Q\mu_Q)}}\cdot\frac{\Delta m}{A}. \tag{13}$$

Δf is the measured frequency shift, Δm the mass loading, A the piezoelectrically active area, the quartz density ($\rho_Q = 2.648\ g{\cdot}cm^{-3}$) and the shear modulus of AT-cut quartz ($\mu_Q = 2.947 \times 10^{11}$ dyn cm^{-2}). The sensitivity factor increases at high resonant frequency of the resonator which corresponds to a thinner quartz crystal; for example a 10 MHz AT-cut quartz crystal 0.017 cm thick has a nominal sensitivity of 0.226 Hz $cm^2{\cdot}ng^{-1}$.

For acoustically thin films ($R \to 0$), the equivalent of Eq. (13) is as follows:

$$\Delta(\omega L) = \Delta X_L = -\frac{\pi Z_Q \Delta f}{f_o} = \frac{2\pi Z_Q \Delta m}{\sqrt{(\rho_Q\mu_Q)A}} = 4.6\times10^{-8}\frac{\Delta m}{A} \tag{14}$$

with the conversion factor $4.6 \times 10^{-8}\ g{\cdot}cm^{-2}\ \Omega^{-1}$ calibrated by electrodepositing copper on Au and the deposited mass calculated from the number of moles deposited with the Faraday law of electrolysis and the molar mass.

3. Results and discussion

During the oxygen reduction reaction (ORR) on Au in $LiPF_6$/DMSO solution, acoustic admittance spectra were recorded at 1.5 s intervals.

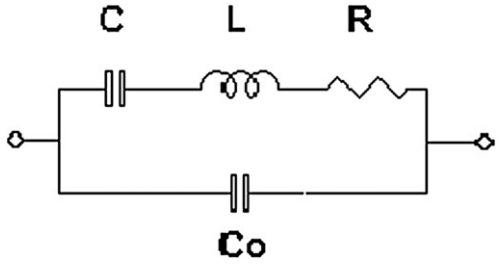

Fig. 1. BVD electrical equivalent circuit Co(LCR) for the quartz crystal resonator.

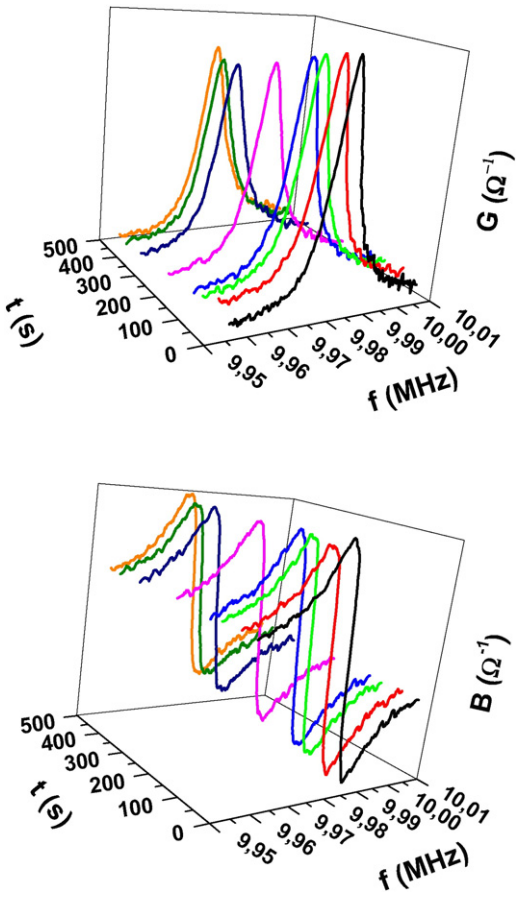

Fig. 2. Conductance (G) and susceptance (B) vs. frequency plots for a 10 MHz Au covered quartz crystal in contact with O_2 saturated 0.1 M $LiPF_6$/DMSO at different times after application of cathodic and anodic 50 μA·cm^{-2} current pulses.

Fig. 2 exhibits the quartz crystal admittance plots, G(ω) and B(ω) around the resonant fundamental resonant frequency of an AT-cut 10 MHz quartz crystal covered with Au electrodes on both sides and immersed on one side in 0.1 M $LIPF_6$/DMSO liquid electrolyte. The time evolution of G and B vs. frequency plots after application of a -50 μA·cm^{-2} current pulse for 335 s followed by an anodic 50 μA·cm^{-2} current pulse during 120 s is displayed in Fig. 2. Progressive damping (energy loss) of the admittance curves, shift to lower frequencies and the increase in the full width at half maximum (FWHM) during the O_2 cathodic reduction is due to the formation of an insoluble Li_2O_2 deposit on the surface. For several current densities a different time evolution of the admittance-frequency curves has been observed and the maximum conductance (1/R) decreases as the oxygen reduction proceeds but then increases during the oxidation cycle. Simultaneous non-linear fit of experimental G and B vs. frequency curves to Eq. (11) with C = 30 fF and Co = 1 pF determined for the bare quartz crystal in air, yields values of L and R at different times.

Fig. 3A shows the Au electrode potential evolution while the ± 50 μA·cm^{-2} current pulses are applied: During the ORR the electrode potential evolves rapidly to 2.45 V. For the anodic current a very large over potential was needed and the Au electrode potential reached 4.03 V. The simultaneous recording of Δ(ωL) and ΔR shows an increase of these imaginary and real components of the quartz crystal impedance in contact with the liquid non-aqueous electrolyte with respect to their initial values previous to the application of the current pulses (Fig. 3B).

The change in real and imaginary components of the surface quartz impedance Δ(ωL) and ΔR depend on the mass per unit area of deposit, its thickness and the viscoelastic properties of the deposited crystal load, as well as surface roughness because some solvents is entrapped and also from friction of the protruding surface deposit and the solvent [33]. Homogeneous thin films result in low motional R while thick and rough deposits yield large R values.

Fig. 4 depicts the corresponding typical resonant frequency shift and areal mass evolution (from Eqs. (13) and (14)) after the application of cathodic and anodic 50 μA·cm^{-2} current pulses. It is worth mentioning that at short time there is a delay in the mass growth with the ORR charge and the mass remains almost constant for 150 s in Fig. 4; then there is appreciable increase in the mass due to the formation of insoluble solid Li_2O_2 deposit. The time lag to record mass increase is due to the formation of soluble LiO_2 at the electrode surface which has been detected with the RRDE in short term transient peaks [25,28]. At longer times the soluble LiO_2 may disproportionate to form insoluble Li_2O_2 on nucleation sites with the corresponding added mass (solution phase mechanism). The simultaneous increase of ΔR is predicted from Eqs. (7) and (8) when the surface film thickness increases. Upon inverting the current polarity both Δm and ΔR decrease with recovery of initial mass at very high over potential, c.a. 4.5 V.

The EQCM gravimetric study shows that the dynamics of the O_2 reduction and evolution reactions strongly depends on the current density as shown in Fig. 5 for typical constant current pulses. Surprisingly, at higher current rate (100 μA·cm^{-2}) Δm = 3 μg·cm^{-2} (9.0 mC·cm^{-2} in 90 s), while at a lower current density (50 μA·cm^{-2}), a larger mass is observed, i.e. Δm = 11 μg·cm^{-2} (18 mC·cm^{-2} in 360 s). It should be also noticed a difference in the initial time lags for the mass increase, i.e. 30 s at high current density and 130 s at lower 50 μA·cm^{-2}; this time lag correlates to the initial high soluble lithium superoxide flux burst detected with the RRDE [25,28]. These results can be rationalized from the different possible mechanisms for ORR in lithium containing electrolytes in high donor number solvents: At high current rate a surface mechanism has been described while at low current rate a solution mechanism dominates [18,19].

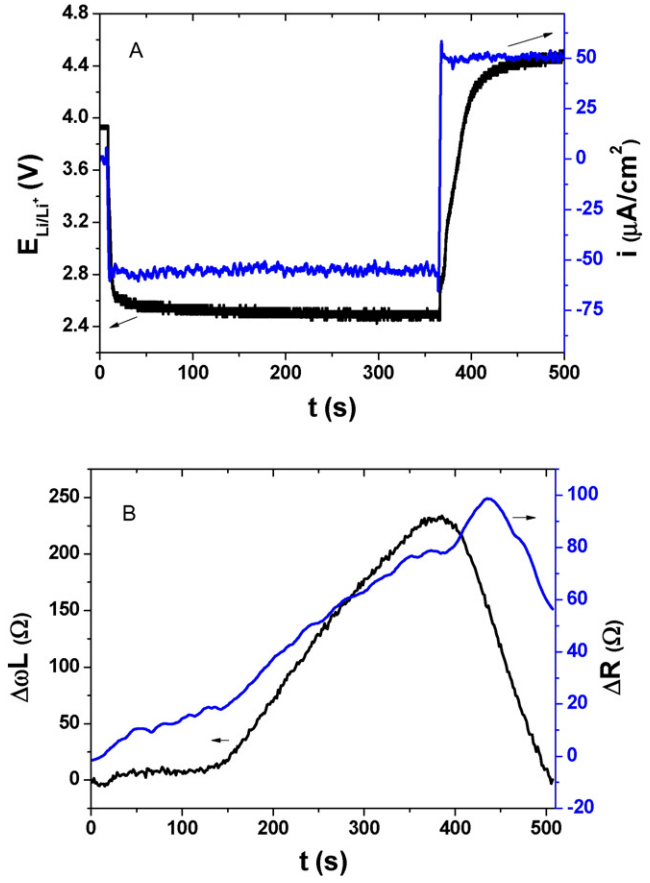

Fig. 3. A. Current pulses (±50 μA·cm^{-2}) and simultaneous electrode potential evolution. B. Time evolution of Δ(ωL) and ΔR recorded simultaneously to the current pulses.

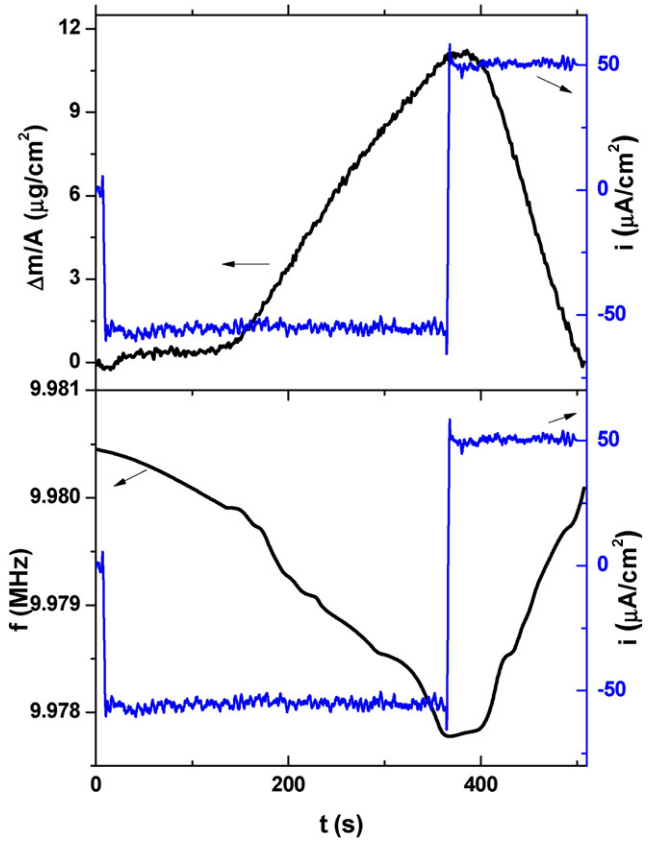

Fig. 4. Quartz crystal resonant frequency shift and Δm/A evolution during the current pulses of Fig. 3.

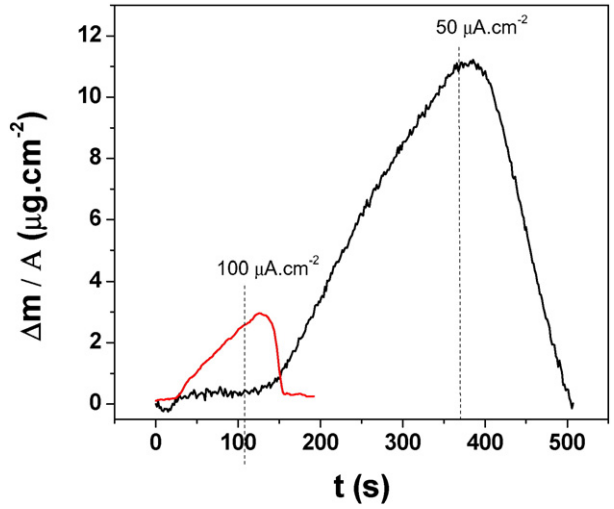

Fig. 5. Time evolution of Δm/A for 50 and 100 μA·cm^{-2}. Dotted lines show current inversion to anodic pulse.

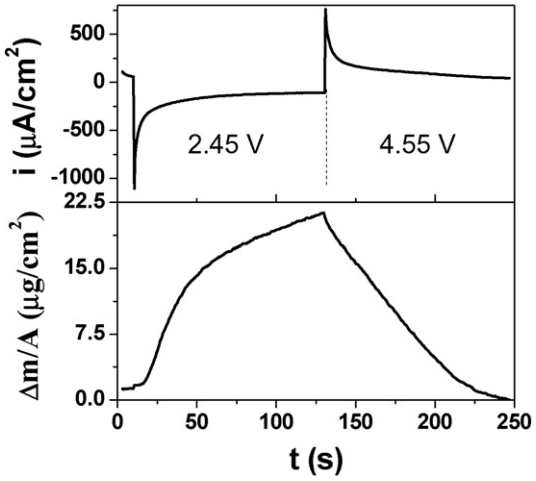

Fig. 6. Chronoamperometry of O_2 reduction reaction (ORR) on Au in DMSO/0.1 M $LiPF_6$ at 2.45 V and oxidation at 4.55 V (upper panel); simultaneous EQCM mass per unit area (lower panel).

Thus we disclose here for the first time gravimetric evidence with the EQCM of the different mechanistic models that apply to the ORR in $LiPF_6$/DMSO electrolyte: The time course and amount of O_2 reduction products deposited on Au depend in a complex manner of the competing surface and solution phase mechanisms.

With the EQCM derived mass (Δm) and the charge (Q) obtained by current integration, the mass-to-charge ratio (mass per mole of electrons, mpe) can be calculated as mpe = Δm · zF / Q (z is the number of electrons transferred). The EQCM is a unique technique to assess the mpe and therefore to distinguish the molar mass of the deposited products on the electrode, including ions and neutrals like solvent.

The mass deposited per Faraday of charge depends strongly on the experimental conditions, for instance at high current density (100 μA·cm^{-2}) mpe = 25–30 g·mol^{-1} was found, close to the theoretical value 23 g·mol^{-1} expected from sequential reactions (1–2) or (1–3). At lower current density (50 μA·cm^{-2}), the mpe rises to 91 g·mol^{-1} and further above 100 g·mol^{-1} for 5 μA·cm^{-2}.

On the basis of preliminary EQCM results, we have recently proposed the co-deposition of DMSO or its decomposition products simultaneous to the ORR in $LiPF_6$ in this solvent that highly coordinates Li^+ [28,37]. At high current rate, less mass is deposited because of effective Au surface passivation by a thin lithium peroxide non-conductive film, while at lower current rate soluble LiO_2 in low surface concentration diffuses away into the electrolyte solution rather than disproportionate at the surface into insoluble thin Li_2O_2 passivating film. This favors the solution phase mechanism with formation of large disc or toroidal particles from aggregation of Li_2O_2 nano-crystals from solution [18,20]. In the surface mechanisms Li_2O_2 deposition yields 23 g/F as reported by other authors [14,22,38] while incorporation of DMSO results in mpe values much higher than expected from Eqs. (1)–(5) since solvated LiO_2 diffuses out in solution and precipitates on large Li_2O_2 particles by disproportion (solution phase mechanism).

Fig. 6 compares typical chrono-amperometric curves for the oxygen cathode discharge at 2.45 V and re-charge at 4.55 V with the simultaneous Δm vs. time curves. During ORR at constant potential a delay in the mass uptake with respect to the charge is also observed due to the build-up of soluble LiO_2 surface concentration below the critical value for a massive conversion into Li_2O_2 blocking deposit. Notice that the Au surface is not fully passivated since reduction and oxidation currents after 100 s are still appreciable.

Under the conditions described, a careful analysis of mass to charge ratio during the chrono-amperometric transient shows mpe values in large excess to those expected for a simple mechanism described by Eqs. (1)–(5), ie. 166 and 62 g per Faraday in Fig. 7.

Another technique employed for the study of the electrochemical performance of oxygen cathodes is cyclic voltammetry (CV). In a previous publication on the RRDE study of this system we have shown that in cyclic voltammetry experiments potential and time are convoluted and therefore it is difficult to distinguish the effect of each factor on the electrode kinetics [25]. Fig. 8A depicts a CV for the ORR in O_2 saturated DMSO containing 0.1 M $LiPF_6$ at a scan rate of 20 mV·s^{-1} with a cathodic current maximum at 2.44 V. The corresponding EQCM derived ΔX_L (= ωL) and ΔR simultaneously measured are plotted as a function of the electrode potential in Fig. 8B and C. Notice that the mass does not increase until 2.5 V when the ORR current has already reached 300 μA·cm^{-2} which is consistent with the predominant formation of soluble LiO_2 as found in RRDE experiment in the same potential interval [25]. Both the increase of Δm obtained with Eq. (14) from ΔX_L and ΔR indicate the formation of a massive deposit of oxygen reduction products below 2.44 V, which continues growing slightly in the back scan until 3.0 V.

In the back scan the mass decreases above 3.0 V while anodic current flows; however at this scan rate the mass does not recover the initial value even a 4.5 V since a longer time is needed as found in chronoamperometry (see Fig. 6) or slower scan rate. Even at potentials above the O_2/Li_2O_2 couple only a fraction of mass gained in the cathodic cycle is lost, so there is no balance of the oxygen unless reaching a deep recharge at very positive overpotentials where DMSO is

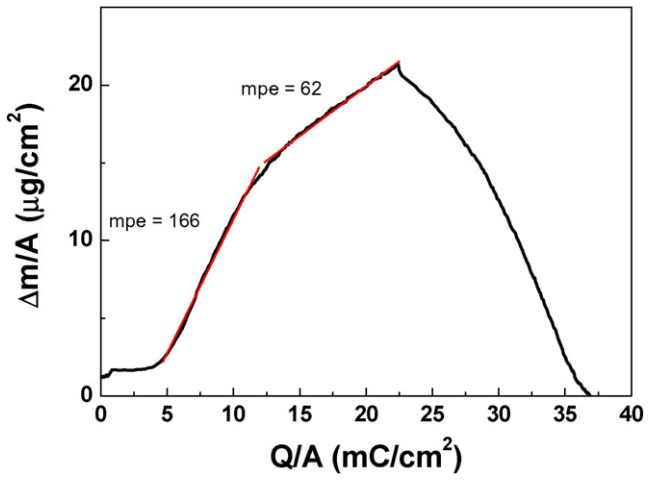

Fig. 7. Plot of Δm vs. ΔQ calculated from data in Fig. 6.

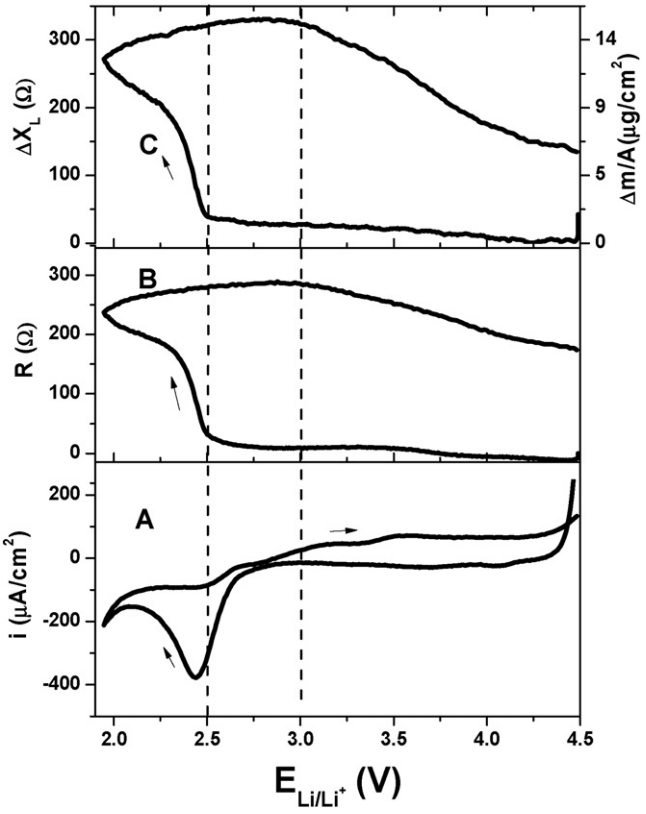

Fig. 8. A. Current–potential plot of Au deposited on quartz crystal in O_2 saturated 0.1 M $LiPF_6$ DMSO solution (157 ppm H_2O) at 20 mV·s^{-1}. Simultaneous variation of ΔR (B) and ΔX_L (C).

electrochemically oxidized, so EQCM confirms DEMS evidence and lithium air batteries typical potential-charge curves.

The mpe values derived from data in Fig. 8 yield 160 and 89 g per Faraday for the mass increase between 2.5 and 2.0 V [28]. These values are much larger than those expected for simple reactions (1–5) and suggests co-deposition of the solvent (78 g/mol for DMSO) which would arise from strong interaction of DMSO-Li^+. It has been reported by Li-7 NMR spectroscopy that four dimethyl sulfoxide molecules solvate Li^+ [39]. Sharon et al. [14] have proposed a mechanism for the

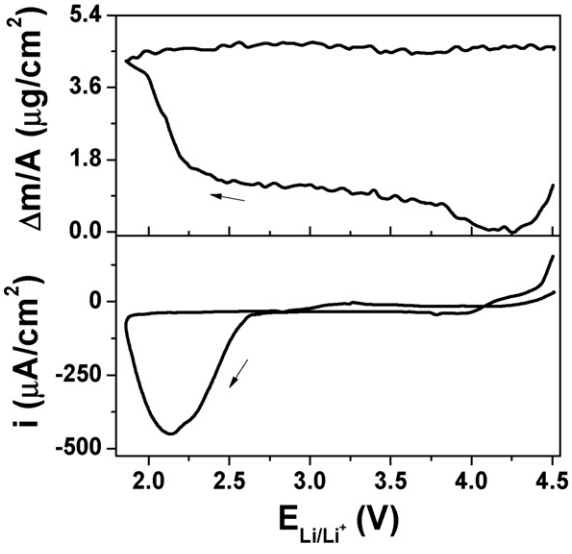

Fig. 9. A. Current–potential plot of Au deposited on quartz crystal in O_2 saturated 0.1 M $LiPF_6$ DMSO solution (30 ppm H_2O) at 20 mV·s^{-1}. B. Simultaneous variation of Δm/A.

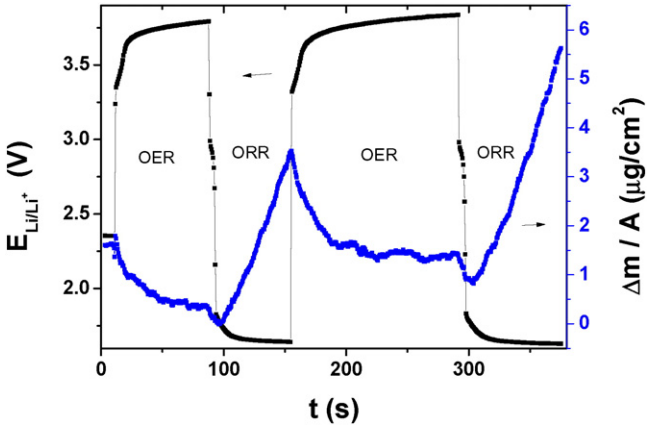

Fig. 10. Electrode potential and Δm/A during 50 μA·cm^{-2} cathodic and anodic galvanostatic pulses for ORR on Au in O_2 saturated 0.1 M $LiPF_6$ acetonitrile solution.

decomposition of DMSO by reaction with LiO_2 and Li_2O_2 with formation of a dimsyl anion-Li^+ ionic pair (84 g/mol) and hydro-peroxyl radical or lithium hydroperoxyl radical anion pair (40 g/mol).

Recent XPS studies of the Au electrode surface after the ORR under similar experimental conditions have shown the presence of carbonate, organic molecules and sulfur from DMSO decomposition as well as LiF and phosphorous compounds from decomposition of PF_6^- [40] These decomposition products would also account for the mass in excess seen in EQCM experiments.

A noticeable feature in Fig. 8 is the lack of Au electrode passivation in the back scan which could be caused by traces of water in DMSO solution inducing a solution phase ORR mechanism as demonstrated by the IBM group to enhance the formation of toroidal Li_2O_2 particles and increase in the cathode capacity (mass) [17]. After the measurement Karl Fischer determination of water yielded 157 ppm.

Another evidence of a massive deposit consisting of large particles protruding in the liquid is the quartz crystal resistance change, ΔR to almost 300 Ω at the maximum mass deposited shown in Fig. 8B compared to low ΔR observed for thin peroxide films. In different experiments the values of ΔR correlate with Δm/A for thin deposits, i.e. ΔR ≈ 1–5 Ω while for thick deposits ΔR reached very large values due to viscoelastic, roughness and friction looses of the shear wave at the interface of the ORR reduction products deposit with asperities and the liquid electrolyte. The larger ΔR, the less accurate the measurement of Δm/A since acoustic thin film conditions are no longer applicable [41].

Conversely, experiments carried out with low water content in the DMSO solution, i.e. 30 ppm, under similar conditions exhibit full passivation of the Au surface and lower mass deposited (cathode capacity) due to the formation of a thin Li_2O_2 film as shown in Fig. 9. The mpe in this case is 41 g per Faraday as expected from Eqs. (1)–(5) with no solvent co-deposition. The variability of quartz crystal microbalance reported by different authors [14,22,38] can be explained by the different ORR mechanisms in non-aqueous lithium electrolyte solutions in solvents of different Li^+ ion stabilization capacity, different current densities or trace amounts of water.

Unlike DMSO, in low donor number acetonitrile (ACN) solvent, soluble superoxide could not be detected in solution [12,24], given the poor solvation capacity of ACN for Li^+ [37]. The ORR in ACN lithium containing solutions proceeds by the surface reaction mechanism [19]. Therefore for comparison Fig. 10 shows the time evolution of the electrode potential and the simultaneous areal mass detected with the EQCM that result from high current density pulses (250 μA·cm^{-2}) applied to a Au coated quartz crystal immersed in O_2 saturated 0.1 M $LiPF_6$ in acetonitrile. Several important differences with respect to similar experiments using DMSO (see Fig. 3) can be described.

The deposited mass grows linearly with time (charge) from the beginning of the ORR pulse and no time delay between mass and charge

has ever been observed as in case of the solvent DMSO. The constant slope yields an mpe very close to 23 g per Faraday in repetitive pulses. Few micrograms of Li_2O_2 are deposited and the mass increases proportionally with current densities as expected for a compact thin film. Notice that upon oxidation the electrode potential never reaches 4.0 V in the anodic pulses and both AFM and XPS confirm a residual deposit after full oxidation consistent with mass accumulation at the Au surface in successive scans.

4. Conclusions

The EQCM is a powerful technique for the study of the ORR in non-aqueous lithium containing electrolytes with a solid non-conductive reaction product, Li_2O_2 in lithium-air battery cathodes. The gravimetric results demonstrate that soluble LiO_2 produced in the first electron transfer to molecular oxygen does not contribute to the mass gained and only when it yields Li_2O_2 either by bimolecular disproportion or a second electron transfer step the EQCM detects mass load increase on the quartz crystal. A time delay between the onset of the mass increase and the cathodic charge is due to the solubility of LiO_2 in DMSO, which is not observed when acetonitrile is used as solvent. This is in coincidence with previous results with the RRDE.

The magnitude of the Li_2O_2 mass deposited per unit area and the variation in shear wave energy losses (ΔR) depends on the experimental conditions i.e. solvent, current density, amount of traces of water, scan rate or deposition time. These discrepancies are due to the possibility of different mechanisms that apply to the ORR in $LiPF_6$/DMSO electrolyte: (i) Surface thin Li_2O_2(s) films from electrochemical/chemical deposition, and (ii) solution phase disproportion of soluble LiO_2 in DMSO that produces large Li_2O_2 disc or toroidal particles. The mass per electron (mpe) detected with the EQCM depends on the respective current rates and thus on the mechanisms, i.e. 23 g/F for the formation of Li_2O_2 thin film at high current density and much larger values for low current density or large amounts of water due to solvent co-deposition and further degradation.

Acknowledgment

Funding from CONICET and ANPCyT PICT 2012 No. 1452 and FS-Nano 07 and research doctoral and postdoctoral fellowships from CONICET by WRT and AYT, and from ANCPCyT (M. del P) are gratefully acknowledged.

References

[1] S.A. Freunberger, Y. Chen, Z. Peng, J.M. Griffin, L.J. Hardwick, F. Barde, P. Novak, P.G. Bruce, Reactions in the rechargeable lithium-O-2 battery with alkyl carbonate electrolytes, J. Am. Chem. Soc. 133 (2011) 8040–8047.
[2] P.G. Bruce, S.A. Freunberger, L.J. Hardwick, J.-M. Tarascon, Li-O-2 and Li-S batteries with high energy storage, Nat. Mater. 11 (2012) 19.
[3] J. Christensen, P. Albertus, R.S. Sanchez-Carrera, T. Lohmann, B. Kozinsky, R. Liedtke, J. Ahmed, A. Kojic, A critical review of Li/Air batteries, J. Electrochem. Soc. 159 (2012) R1–R30.
[4] L.J. Hardwick, P.G. Bruce, The pursuit of rechargeable non-aqueous lithium-oxygen battery cathodes, Curr. Opin. Solid State Mater. Sci. 16 (2012) 178–185.
[5] K.M. Abraham, Lithium-air and other batteries beyond lithium-ion batteries, in: K.M.A. Bruno Scrosati, Walter van Schalkwijk, Jusef Hassoun (Eds.), Lithium Batteries: Advanced Technologies and Applications, John Wiley & Sons, Inc., 2013
[6] K.M. Abraham, Z. Jiang, A polymer electrolyte-based rechargeable lithium/oxygen battery, J. Electrochem. Soc. 143 (1996) 1–5.
[7] C.O. Laoire, S. Mukerjee, E.J. Plichta, M.A. Hendrickson, K.M. Abraham, Studies of Li-air cells utilizing dimethyl sulfoxide-based electrolyte, J. Electrochem. Soc. 158 (2011) A302–A308.
[8] C.O. Laoire, S. Mukerjee, K.M. Abraham, E.J. Plichta, M.A. Hendrickson, Influence of nonaqueous solvents on the electrochemistry of oxygen in the rechargeable lithium-air battery, J. Phys. Chem. C 114 (2010) 9178–9186.
[9] T. Ogasawara, A. Debart, M. Holzapfel, P. Novak, P.G. Bruce, Rechargeable Li_2O_2 electrode for lithium batteries, J. Am. Chem. Soc. 128 (2006) 1390–1393.
[10] Z. Peng, S.A. Freunberger, Y. Chen, P.G. Bruce, Reversible and higher-rate Li-O-2 battery, Science 337 (2012) 563–566.
[11] D. Xu, Z.-L. Wang, J.-J. Xu, L.-L. Zhang, X.-B. Zhang, Novel DMSO-based electrolyte for high performance rechargeable Li-O-2 batteries, Chem. Commun. 48 (2012) 6948–6950.
[12] M.J. Trahan, S. Mukerjee, E.J. Plichta, M.A. Hendrickson, K.M. Abraham, Studies of Li-air cells utilizing dimethyl sulfoxide-based electrolyte, J. Electrochem. Soc. 160 (2013) A259–A267.
[13] B.D. McCloskey, A. Valery, A.C. Luntz, S.R. Gowda, G.M. Wallraff, J.M. Garcia, T. Mori, L.E. Krupp, Combining accurate O-2 and Li_2O_2 assays to separate discharge and charge stability limitations in nonaqueous Li-O-2 batteries, J. Phys. Chem. Lett. 4 (2013) 2989–2993.
[14] D. Sharon, M. Afri, M. Noked, A. Garsuch, A.A. Frimer, D. Aurbach, Oxidation of dimethyl sulfoxide solutions by electrochemical reduction of oxygen, J. Phys. Chem. Lett. 4 (2013) 3115–3119.
[15] R. Younesi, M. Hahlin, F. Bjorefors, P. Johansson, K. Edstrom, Li-O-2 battery degradation by lithium peroxide (Li_2O_2): a model study, Chem. Mater. 25 (2013) 77–84.
[16] M. Safari, B.D. Adams, L.F. Nazar, Kinetics of oxygen reduction in aprotic Li-O-2 cells: a model-based study, J. Phys. Chem. Lett. 5 (2014) 3486–3491.
[17] N.B. Aetukuri, B.D. McCloskey, J.M. Garcia, L.E. Krupp, V. Viswanathan, A.C. Luntz, Solvating additives drive solution-mediated electrochemistry and enhance toroid growth in non-aqueous Li-O-2 batteries, Nat. Chem. 7 (2015) 50–56.
[18] B.D. Adams, C. Radtke, R. Black, M.L. Trudeau, K. Zaghib, L.F. Nazar, Current density dependence of peroxide formation in the Li-O-2 battery and its effect on charge, Energy Environ. Sci. 6 (2013) 1772–1778.
[19] L. Johnson, C. Li, Z. Liu, Y. Chen, S.A. Freunberger, P.C. Ashok, B.B. Praveen, K. Dholakia, J.-M. Tarascon, P.G. Bruce, The role of LiO_2 solubility in O-2 reduction in aprotic solvents and its consequences for Li-O-2 batteries, Nat. Chem. 7 (2014) 87-87 Vol 6, pg 1091, 2014.
[20] R.R. Mitchell, B.M. Gallant, Y. Shao-Horn, C.V. Thompson, Mechanisms of morphological evolution of Li_2O_2 particles during electrochemical growth, J. Phys. Chem. Lett. 4 (2013) 1060–1064.
[21] B.M. Gallant, D.G. Kwabi, R.R. Mitchell, J. Zhou, C.V. Thompson, Y. Shao-Horn, Influence of Li_2O_2 morphology on oxygen reduction and evolution kinetics in Li-O-2 batteries, Energy Environ. Sci. 6 (2013) 2518–2528.
[22] X. Jie, K. Uosaki, Electrochemical quartz crystal microbalance study on the oxygen reduction reaction in Li^+ containing DMSO solution, J. Electroanal. Chem. 716 (2014) 49–52.
[23] D. Sharon, V. Etacheri, A. Garsuch, M. Afri, A.A. Frimer, D. Aurbach, On the challenge of electrolyte solutions for Li-air batteries: monitoring oxygen reduction and related reactions in polyether solutions by spectroscopy and EQCM, J. Phys. Chem. Lett. 4 (2013) 127–131.
[24] E.J. Calvo, N. Mozhzhukhina, A rotating ring disk electrode study of the oxygen reduction reaction in lithium containing non aqueous electrolyte, Electrochem. Commun. 31 (2013) 56–58.
[25] W.R. Torres, N. Mozhzhukhina, A.Y. Tesio, E.J. Calvo, A rotating ring disk electrode study of the oxygen reduction reaction in lithium containing dimethyl sulfoxide electrolyte: role of superoxide, J. Electrochem. Soc. 161 (2014) A2204–A2209.
[26] C.O. Laoire, S. Mukerjee, K.M. Abraham, E.J. Plichta, M.A. Hendrickson, Elucidating the mechanism of oxygen reduction for lithium-air battery applications, J. Phys. Chem. C 113 (2009) 20127–20134.
[27] N. Mozhzhukhina, M.P. Longinotti, H.R. Corti, E.J. Calvo, A conductivity study of preferential solvation of lithium ion in acetonitrile-dimethyl sulfoxide mixtures, Electrochimica. Acta 154 (2015) 456–461.
[28] W.R. Torres, A.Y. Tesio, E.J. Calvo, Solvent co-deposition during oxygen reduction on Au in DMSO LiPF6, Electrochem. Commun. 49 (2014) 38–41.
[29] J.M. Tarascon, D. Guyomard, Li metal-free rechargeable batteries based on Li1 + xMn2O4 cathodes ($0 \le x \le 1$) and carbon anodes, J. Electrochem. Soc. 138 (1991) 2864–2868.
[30] H.L. Bandey, A.R. Hillman, M.J. Brown, S.J. Martin, Viscoelastic characterization of electroactive polymer films at the electrode/solution interface, Faraday Discuss. 107 (1997) 105–121.
[31] R. Lucklum, D. Soares, K.K. Kanazawa, Models for resonant sensors, in: A. Arnau (Ed.), Piezoelectric Transducers and Applications, Springer-Verlag, Berlin 2008, pp. 63–96.
[32] S.J. Martin, V.E. Granstaff, G.C. Frye, Characterization of a quartz crystal microbalance with simultaneous mass and liquid loading, Anal. Chem. 63 (1991) 2272–2281.
[33] A. Arnau, Y. Jimenez, R. Fernández, R. Torres, M. Otero, E.J. Calvo, Viscoelastic characterization of electrochemically prepared conducting polymer films by impedance analysis at quartz crystal study of the surface roughness effect on the effective values of the viscoelastic properties of the coating, J. Electrochem. Soc. 153 (2006) C455–C466.
[34] V.E. Granstaff, S.J. Martin, Characterization of a thickness-shear mode quartz resonator with multiple nonpiezoelectric layers, J. Appl. Phys. 75 (1994) 1319–1329.
[35] E.J. Calvo, E.S. Forzani, M. Otero, Study of layer-by-layer self-assembled viscoelastic films on thickness-shear mode resonator surfaces, Anal. Chem. 74 (2002) 3281–3289.
[36] G.Z. Sauerberey, Z. Phys. 155 (1959) 206.
[37] R. Semino, G. Zaldívar, E.J. Calvo, D. Laria, Lithium solvation in dimethyl sulfoxide–acetonitrile mixtures, J. Chem. Phys. 141 (2014).
[38] S. Schaltin, G. Vanhoutte, M. Wu, F. Bardé, J. Fransaer, A QCM study of ORR-OER and an in situ study of a redox mediator in DMSO for Li-O_2 batteries, Phys. Chem. Chem. Phys. 17 (2015) 12575–12586.
[39] E. Pasgreta, R. Puchta, M. Galle, N. Van Eikema Hommes, A. Zahl, R. Van Eldik, Ligand-exchange processes on solvated lithium cations: DMSO and water/DMSO mixtures, ChemPhysChem 8 (2007) 1315–1320.
[40] F. Marchini, S. Herrera, W.R. Torres, A.Y. Tesio, F.J. Williams, E.J. Calvo, Surface study of oxygen cathodes on Au in different solvent–electrolyte pairs Langmuir, 2015 http://dx.doi.org/10.1021/acs.langmuir.5b02130 (in press).
[41] E.J. Calvo, R. Etchenique, P.N. Bartlett, K. Singhal, C. Santamaria, Quartz crystal impedance studies at 10 MHz of viscoelastic liquids and films, Faraday Discuss. 107 (1997) 141–157.